# Thermodynamic Characteristic for a Correlated Flat-Band System with a Quantum Anomalous Hall Ground State

Gaopei Pan,[1,2] Xu Zhang,[3] Hongyu Lu,[3] Heqiu Li,[4] Bin-Bin Chen,[3] Kai Sun,[5,*] and Zi Yang Meng[3,†]

[1]*Beijing National Laboratory for Condensed Matter Physics and Institute of Physics, Chinese Academy of Sciences, Beijing 100190, China*

[2]*School of Physical Sciences, University of Chinese Academy of Sciences, Beijing 100049, China*

[3]*Department of Physics and HKU-UCAS Joint Institute of Theoretical and Computational Physics, The University of Hong Kong, Pokfulam Road, Hong Kong SAR, China*

[4]*Department of Physics, University of Toronto, Toronto, Ontario M5S 1A7, Canada*

[5]*Department of Physics, University of Michigan, Ann Arbor, Michigan 48109, USA*

(Received 17 July 2022; accepted 7 December 2022; published 3 January 2023)

While the ground-state phase diagram of the correlated flat-band systems has been intensively investigated, the dynamic and thermodynamic properties of such lattice models are less explored, but it is the latter which is most relevant to the experimental probes (transport, quantum capacitance, and spectroscopy) of the quantum moiré materials such as twisted bilayer graphene. Here we show, by means of momentum-space quantum Monte Carlo and exact diagonalization, in chiral limit there exists a unique thermodynamic characteristic for the correlated flat-band model with interaction-driven quantum anomalous Hall (QAH) ground state, namely, the transition from the QAH insulator to the metallic state takes place at a much lower temperature compared with the zero-temperature single-particle gap generated by the long-range Coulomb interaction. Such low transition temperature comes from the proliferation of excitonic particle-hole excitations, which transfers the electrons across the gap between different topological bands to restore the broken time-reversal symmetry and gives rise to a pronounced enhancement in the charge compressibility. Future experiments, to verify such generic thermodynamic characteristics, are proposed.

DOI: 10.1103/PhysRevLett.130.016401

*Introduction.*—Quantum moiré systems, bestowed with the quantum metric of wave functions—manifested in the distribution of Berry curvature in the flat bands—and strong long-range Coulomb interactions, exhibit a rich quantum phase diagram including correlated insulating, unconventional metallic, and superconducting phases, thanks to the high tunability by twisting angles, gating, and tailored design of the dielectric environment [1–39]. In addition to this complex ground-state phase diagram with possibly different pairing mechanism and symmetry breaking patterns [9,40–43], recent theoretical studies [14,32,44–46] indicate that correlated flat bands also exhibit unique dynamic and thermodynamic responses, fundamentally different from conventional correlated electron lattice model systems, such as the Hubbard-type model.

Previous results [44] based on a real-space effective model [47–49] for twisted bilayer graphene (TBG) at 3/4 filling, via density matrix renormalization group computation, successfully identify a quantum anomalous Hall (QAH) state as the long-sought-after topological Mott insulator (TMI) [50–52], as the ground state of the interaction-only system spontaneously breaks the time-reversal symmetry and acquires a finite Chern number. Then by means of thermal tensor network and the perturbative field-theoretical approaches [45], the finite-$T$ phase diagram and the dynamical properties of the real-space TBG model have been revealed, which contains the QAH and charge density wave insulators at low $T$, and an Ising transition separating them from the high-$T$ symmetric phases. Because of the proliferation of excitons—particle-hole bound states—this phase transition takes place at a significantly reduced temperature than the mean-field estimation of the topological band gap. Between these two energy scales, an exciton-proliferated phase is observed, which acquires distinctive experimental signatures in charge compressibility and optical conductivities close to the transition [45].

Although the aforementioned real-space effective lattice models offer a clear physics picture and important insights, obvious limitations such as the absence of the quantum metric of the quantum wave function and the truncation of the long-range Coulomb interaction make it a nontrivial task to directly connect these model calculations with realistic quantum moiré materials. The effects of the long-range Coulomb interaction in the narrow bands of TBG have been discussed in many works [36,37], and the overall energy scale of $U$ and the strength of $\alpha$, which controls the relative strength between the cluster charging and assisted hopping interactions in the real-space model, are largely unknown. For this purpose, unbiased

 

computations of the Bistritzer-MacDonald (BM) continuum model [1–3], originated from the flat-bands in momentum space and subjected to the truly long-range Coulomb interactions, are highly desirable to explore the thermodynamic characteristic of the correlated flat-band systems and provide guidance to future experiments.

In this Letter, we employ the momentum-space quantum Monte Carlo (QMC) method [53–56], supplemented with exact diagonalization (ED) [57], to systematically investigate the thermodynamic properties of the continuum correlated flat-band TBG model at 3/4 filling. We find that in analogy to its real-space cousin, the continuum model also exhibits two distinct temperature scales, i.e., the $T = 0$ ground state is a topologically nontrivial QAH-TMI phase with a large gap $\Delta \sim 17$ meV; this topological phase melts at only $T_c \sim 4$ meV, through a continuous phase transition that belongs to the Ising universality class. At intermediate temperature $T_c < T < \Delta$, excitonic collective excitations transfer valence electrons across the topological band gap to the opposite Chern bands and restore the broken time-reversal symmetry. Such a process generates pronounced enhancement in the charge compressibility, readily detectable via the quantum capacitance measurements [22,58]. The associated temperature dependence of the electronic spectral function $A(\mathbf{k}, \omega)$ is also obtained with scrutiny. Our Letter therefore confirms the unique thermodynamic characteristic of the correlated flat-band systems, offers a mechanism for the smearing of the many-electron state topology by proliferating collective exciton excitations, and opens an avenue for controlled many-body computation on finite-temperature states in quantum moiré systems.

*Model and method.*—We construct the continuum model for the magic angle TBG with flat bands and long-range Coulomb interaction, following the convention used in Refs. [1–5,18,59–61]. The Hamiltonian of the BM model in the plane wave basis is

$$H_{\mathrm{BM},\mathbf{k},\mathbf{k}'} = \delta_{\mathbf{k},\mathbf{k}'}\begin{pmatrix} -\hbar v_F(\mathbf{k}-\mathbf{K}_1^+)\cdot\boldsymbol{\sigma} & U_0 \\ U_0^\dagger & -\hbar v_F(\mathbf{k}-\mathbf{K}_2^+)\cdot\boldsymbol{\sigma} \end{pmatrix} + \begin{pmatrix} 0 & U_1\delta_{\mathbf{k},\mathbf{k}'-\mathbf{G}_1} + U_2\delta_{\mathbf{k},\mathbf{k}'-(\mathbf{G}_1+\mathbf{G}_2)} \\ U_1^\dagger\delta_{\mathbf{k},\mathbf{k}'+\mathbf{G}_1} + U_2^\dagger\delta_{\mathbf{k},\mathbf{k}'+(\mathbf{G}_1+\mathbf{G}_2)} & 0 \end{pmatrix}. \tag{1}$$

Here we only consider one valley and one spin, where the Pauli matrices $\boldsymbol{\sigma} = (\sigma_x, \sigma_y)$ are from the A, B sublattices of the monolayer graphene. $\mathbf{G}_1$ and $\mathbf{G}_2$ are the reciprocal vectors of moiré Brillouin zone (MBZ) as shown in Fig. 1(a). $\mathbf{K}_1^\tau$ and $\mathbf{K}_2^\tau$ are the Dirac points of the bottom and top graphene layers respectively, which are twisted by the angles $\mp(\theta/2)$. The interlayer tunneling between the Dirac states is described by the matrices $U_0 = \left(\begin{smallmatrix} u_0 & u_1 \\ u_1 & u_0 \end{smallmatrix}\right)$, $U_1 = \left(\begin{smallmatrix} u_0 & u_1 e^{-(2\pi/3)i} \\ u_1 e^{(2\pi/3)i} & u_0 \end{smallmatrix}\right)$, and $U_2 = \left(\begin{smallmatrix} u_0 & u_1 e^{(2\pi/3)i} \\ u_1 e^{-(2\pi/3)i} & u_0 \end{smallmatrix}\right)$ where $u_0$ and $u_1$ are the intra- and intersublattice interlayer tunneling amplitudes. In this Letter, we consider the chiral limit and leave the nonchiral cases [38,39] in future studies.

The flatness of the lowest two bands in the chiral limit ($u_0 = 0$) is determined by the dimensionless parameter $\alpha = (u_1/\hbar v_F k_\theta)$ with small $\theta$ approximation $k_\theta = 4\pi\theta/(3a_0)$ and the lattice constant of the monolayer graphene $a_0 = 0.246$ nm. In this Letter, we choose $\hbar v_F/a_0 = 2.37745$ eV, the twist angle $\theta = 1.08°$, and $u_1 = 0.11$ eV which leads to the first magic angle where the lowest two bands become completely flat in the chiral limit.

Projecting the long-range Coulomb interaction onto the flat bands, the Hamiltonian becomes

$$H = \frac{1}{2\Omega}\sum_{\mathbf{q},\mathbf{G},|\mathbf{q}+\mathbf{G}|\neq 0} V(\mathbf{q}+\mathbf{G})\delta\rho_{\mathbf{q}+\mathbf{G}}\delta\rho_{-\mathbf{q}-\mathbf{G}} \tag{2}$$

where $V(\mathbf{q}) = (e^2/4\pi\varepsilon)\int d^2\mathbf{r}[(1/\mathbf{r}) - (1/\sqrt{\mathbf{r}^2+d^2})]e^{i\mathbf{q}\cdot\mathbf{r}} = (e^2/2\varepsilon)(1/q)(1-e^{-qd})$ is the long-ranged single gate Coulomb interaction [63] with $d/2$ the distance between the graphene layer and single gate, and $\varepsilon = 7\varepsilon_0$ is the dielectric constant. There are different choices [37,64] of the dielectric constant, and since we consider the chiral and flat-band limits, a different value of $\varepsilon$ will only offer an overall coefficient but not change the physical results. And $\delta\rho_{\mathbf{q}+\mathbf{G}} = \sum_{\mathbf{k},m_1,m_2}\lambda_{m_1,m_2}(\mathbf{k},\mathbf{k}+\mathbf{q}+\mathbf{G})(d^\dagger_{\mathbf{k},m_1}d_{\mathbf{k}+\mathbf{q},m_2} - \frac{1}{2}\delta_{q,0}\delta_{m_1,m_2})$. $m_1, m_2 = 1, 2$ are the band indices. $d^\dagger_{\boldsymbol{k},m}$ is the creation operator for a Bloch eigenstate, $|u_{\boldsymbol{k},m}\rangle$, which is the eigenstate of the BM Hamilton in Eq. (1). The form factor is defined as $\lambda_{m_1,m_2}(\mathbf{k},\mathbf{k}+\mathbf{q}+\mathbf{G}) \equiv \langle u_{\boldsymbol{k},m_1}|u_{\boldsymbol{k}+\mathbf{q}+\mathbf{G},m_2}\rangle$The moiré lattice vector $L_M = [a_0/2\sin(\theta/2)]$, the MBZ reciprocal lattice vector $|\mathbf{G}_0| = (4\pi/\sqrt{3}L_M)$, and the area of system is $\Omega = N_k(\sqrt{3}/2)L_M^2$ with $N_k = L \times L$ the number of $\mathbf{k}$ points in MBZ; for example, $N_k = 36$ for $6 \times 6$ meshes in Fig. 1(a). We use distance $d = 40$ nm and the typical energy scale of $V(|\mathbf{q}|)/2\Omega$ for $L = 6$ as shown in Fig. 1(b).

To compute the dynamic and thermodynamic properties of the TBG model in Eq. (2), we employ the recently developed momentum space QMC method [53,55], which can fully incorporate the flat-band topological wave function and the long-range Coulomb interaction and our *sign bound theory* can prove there is at most a polynomial sign

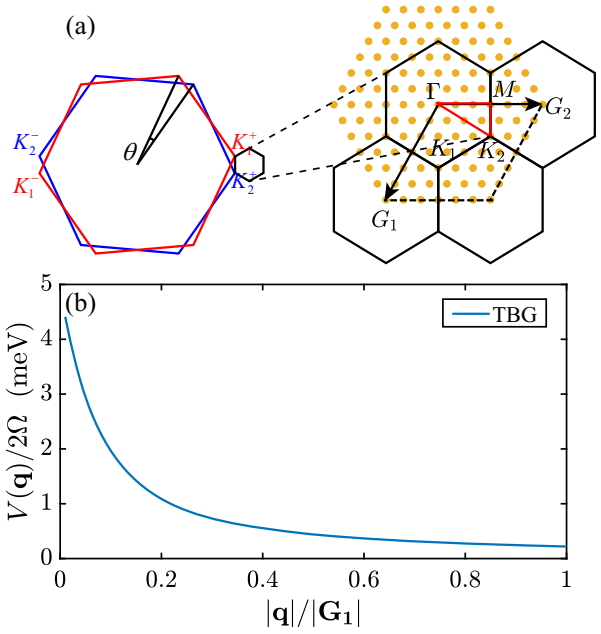


FIG. 1. (a) Schematic TBG setting in momentum space and its moiré Brillouin zone (mBZ) at one valley. The red solid line marks the high-symmetry path $\Gamma - M - K_1(K_2) - \Gamma$. $\mathbf{G}_1$ and $\mathbf{G}_2$ are the reciprocal lattice vectors of the mBZ. Yellow dots mark possible momentum transfer in QMC simulations, $\mathbf{q} + \mathbf{G}$. Because the form factor decays exponentially with $\mathbf{G}$ [62] and the decay of single-gate-screened Coulomb interaction is fast (as shown in panel (b)), scatterings with momentum transfer larger than this cut-off are ignored. Here we show a $6 \times 6$ mesh in the mBZ, with 126 allowed momentum transfers. (b) The decay of the single gate Coulomb interaction for the systems with the input parameters in the main text.

problem for QMC at integer fillings [56,65,66], rendering the computational complexity also polynomial. The QMC solves the finite size systems in a path integral of partition function in an unbiased manner, and we have simulated $L = 3, 4, 5, 6$ and $T \in [0.5, 20]$ meV systems. In the QMC simulation, we compute the charge compressibility $\kappa$ as a function of temperature $T$ as $\kappa = (1/n_0 N_k)(d\langle N\rangle/d\mu) = \beta[(\langle N^2\rangle - \langle N\rangle^2)/n_0 N_k]$, where $n_0$ is the particle density, which is $1/2$ at low temperature and $N = \sum_{\mathbf{k}_1, m_1} d^\dagger_{\mathbf{k}_1, m_1} d_{\mathbf{k}_1, m_1}$ is the particle number operator. We also compute the temperature dependence of the spectral functions from the stochastic analytic continuation (SAC) of the imaginary time Green's function from QMC [40,54,67–69]. The topological aspect of the QAH phase can also be seen from the computed Berry curvature below the transition temperature, and from which the Chern number can then be calculated as $C = \sum_\square F_\square$, where $F_\square$ is the Berry curvature in the finite size MBZ obtained from Green's function in the QMC simulations [70,71]. The detailed QMC implementation of the TBG model and the analyses of different physical observables are given in the Supplemental Material [72].

In the chiral limit the two flat moiré bands can be combined into a Chern band basis [59,73,74] such that each band has Chern number 1 or $-1$. More importantly, the wave function overlap between these two bands is exactly zero, indicating the form factor in the Chern basis is

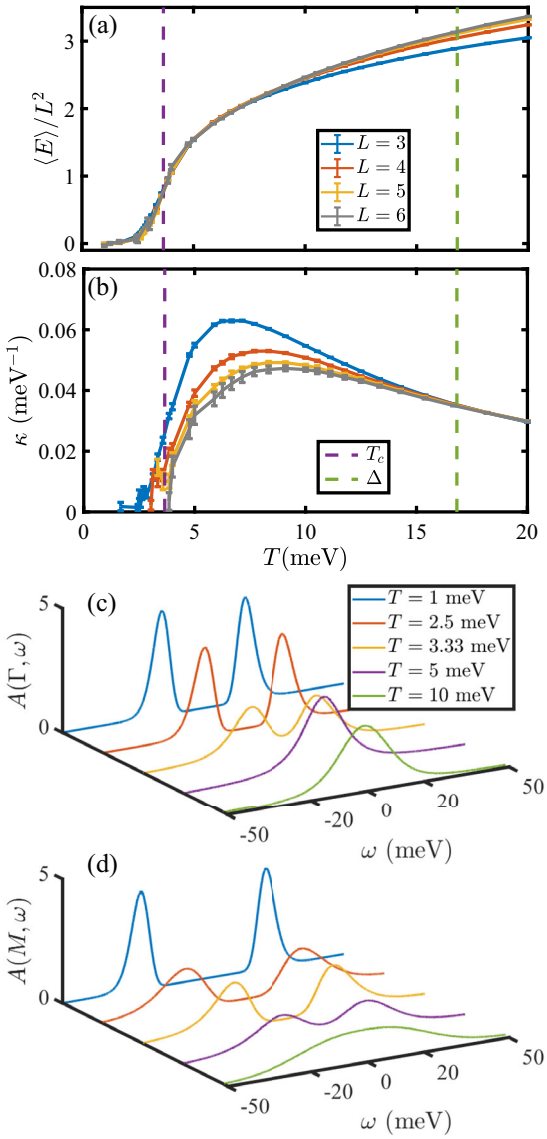


FIG. 2. (a) and (b) The energy density and compressibility $\kappa$ of TBG model in Eq. (2) with $L = 3, 4, 5, 6$ as a function of temperature. The single-particle gap $\Delta$ is denoted as the green dashed line. The QAH transition temperature $T_c$ (determined in Fig. 3 below) is denoted by the purple dashed line. In addition, the peak of average sign here is close to the position of transition temperature $T_c$ (See Sec. III in the Supplemental Material [72] for details). Similar behaviors were seen in Ref. [75]. (c),(d) Single-particle spectral function $A(\mathbf{k}, \omega)$ obtained from QMC-SAC at $\mathbf{k} = \Gamma$ and $M$ with $L = 4$. Below the temperature scale of the single-particle gap, the system remains gapless due to the proliferation of excitons. The spectral gap only arises below the thermal transition temperature, when the system enters the QAH-TMI phase.

diagonal in the band index $\lambda_{mn}(\mathbf{k},\mathbf{k}') \sim \delta_{mn}$. The diagonal form factor gives rise to an emergent conservation law: the conservation of the Chern polarization $P_C$ defined by $P_C = N_+ - N_-$, where $N_\pm$ is the number of electrons in the positive and negative Chern bands respectively and $N_+ + N_- = N$. We note $P_C/N_k$ is the order parameter for the QAH phase, and we compute its correlation functions in the QMC simulation to determine the Ising transition temperature precisely (see Fig. 3). We have also incorporated the ED for the same models, where the single-particle and the exciton gaps for different cluster sizes are computed.

*Results.*—Figures 2(a) and 2(b) show the energy densities and charge compressibility $\kappa$ as a function of temperature. Here we denote the zero-temperature single-particle gap $\Delta \sim 17$ meV and the thermal transition temperature $T_c \sim 4$ meV using the green and purple dashed lines respectively. The gap $\Delta$ is obtained from the exact solution of the chiral limit (see the Supplemental Material [72]). The transition temperature $T_c$, from scaling analysis of the QAH order parameter shown below, is found to be dramatically smaller than $\Delta$. This small $T_c$ is consistent with thermodynamic and dynamic measurements, e.g., the maximum slope in Fig. 2(a), and both the compressibility $\kappa$ and the fermion spectrum function $A(\mathbf{k},\omega)$ at $\mathbf{k} = \Gamma$ and $M$ in Figs. 2(c) and 2(d) all indicate that $T_c$ marks the metal-insulator transition, below which the system becomes incompressible and insulating.

As mentioned above, in the Chern basis, the QAH order parameter is defined as $P_C/N_k$, and its correlation function is

$$S \equiv \frac{\langle (N_+ - N_-)^2 \rangle}{N_k^2} = \frac{1}{N_k^2} \left\langle \left( \sum_{\boldsymbol{k}} d^\dagger_{\boldsymbol{k},+} d_{\boldsymbol{k},+} - \sum_{\boldsymbol{k}} d^\dagger_{\boldsymbol{k},-} d_{\boldsymbol{k},-} \right)^2 \right\rangle. \quad (3)$$

In Fig. 3(a), we plot its temperature dependence. It can be seen that the corresponding order parameters rise at low temperature, which means that spontaneous time-reversal symmetry breaking occurs, and the systems enter the QAH-TMI phase. The thermal phase belongs to the 2D Ising universality class with critical exponents $\beta = 1/8$ and $\nu = 1$. Close to the critical temperature, $S$ is expected to obey the scaling forms $S(T,L) = L^{-2\beta/\nu} f[(T - T_c)L^{1/\nu}]$ where $f$ is the scaling function. In Fig. 3(b), we rescale the data using $S(T,L)L^{2\beta/\nu} = f[(T - T_c)L^{1/\nu}]$, and the

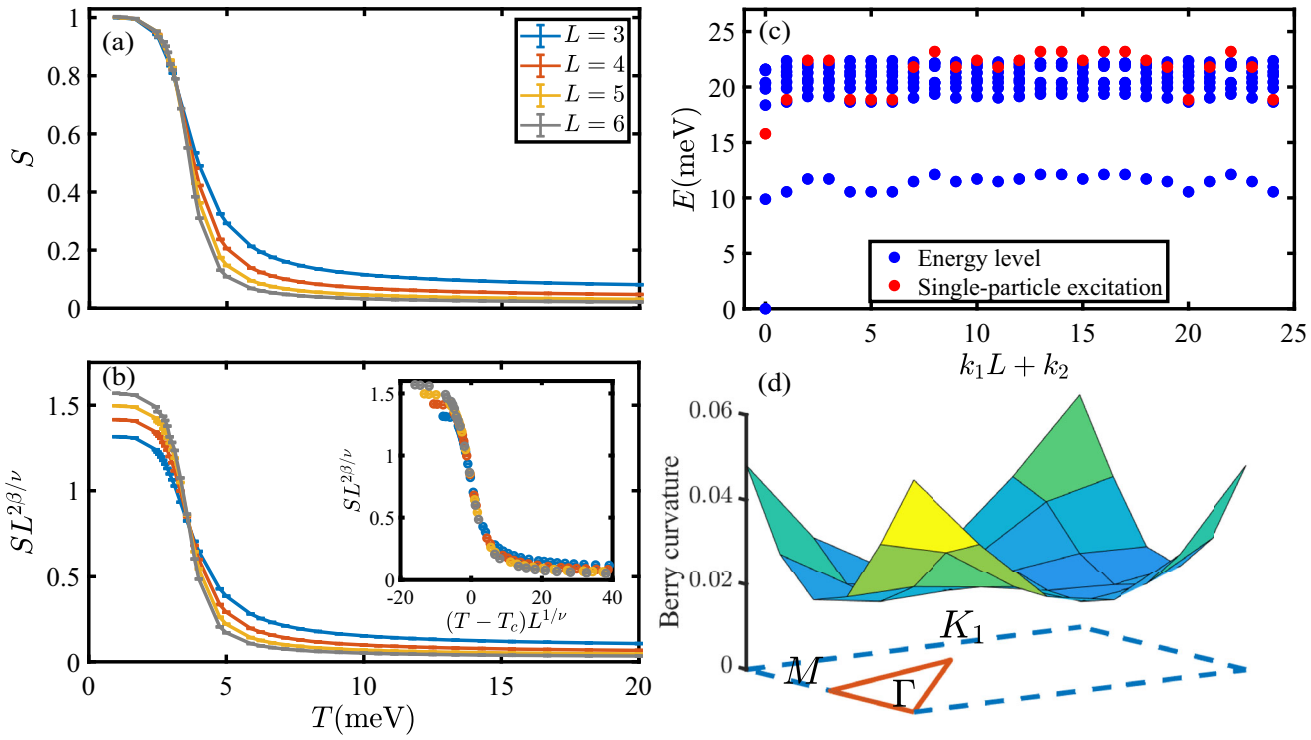


FIG. 3. (a) and (b) Correlation function of the QAH order parameter $S$ versus temperature for $L = 3, 4, 5, 6$ from QMC. The finite-size scaling using 2D Ising exponents determines the thermal transition temperature at $T_c = 3.65(5)$ meV. Inset of (b) shows a perfect data collapse. (c) Energy spectrum of TBG system from exact diagonalization. The blue dots represent the energy of each many-body state with $N_k = 25$ in $5 \times 5$ mesh of mBZ, which include the ground state at zero energy, the low-lying exciton states (~10 meV) and excitations with higher energy. The red dots represent single-particle excitation, which is at much higher energy than that of the collective excitons. Here we use the two integers $k_1$ and $k_2$ to label the momentum points, where $\mathbf{k} = k_1\mathbf{G}_1/L + k_2\mathbf{G}_2/L$. (d) Berry curvature from QMC for $L = 6$ at $T = 1.25$ meV. Chern number $C = \sum_\square F_\square = 1$.

crossing point of different system sizes $L = 3, 4, 5, 6$ gives rise to the transition temperatures $T_c = 3.65(5)$ meV, which corresponds to the purple dashed lines in Figs. 2(a) and 2(b). The inset of Fig. 3(b) shows the perfect data collapse of $S$.

Such a small $T_c$ compared with the interaction-driven single-particle gap at the exact ground state is clearly beyond mean-field physics and indicates the importance of many-body fluctuations. To pinpoint the origin of this low $T_c$, we performed ED simulations and find that it is due to excitonic excitations in the particle-hole channel, which occurs in our system at a much lower energy in comparison to single-particle excitations and thus lowered the $T_c$. Figure 3(c) presents the ED energy spectra, with the blue dots the energy levels with $N_k = 25$ electrons in a $5 \times 5$ mesh. The spectrum for many-body states with Chern polarization $P_C$ is degenerate with those with $-P_C$, and only states with $P_C > 0$ are shown. The ground state has zero energy, and $P_C = N$, which is fully Chern polarized. Low-energy excitations denoted by the blue dots around 10 meV have $P_C = N - 2$, which consists of $N - 1$ electrons in the $N_+$ Chern band and one electron in the $N_-$ Chern band. These states correspond to exciton states in which one of the electrons is excited to the other Chern band from the fully Chern-polarized ground state. The states with lower $P_C$ appear in higher energy in the spectrum. The red dots represent the single-particle excitation, which is obtained from ED computation for a system of the same size and with $N + 1$ electrons, and is consistent with the exact gap size $\Delta \sim 17$ meV. For particle-hole excitations (blue dots), although most of them are at energy close to (or higher than) single-particle excitations, one exciton branch arises at very low energy below the single-particle gap. These excitons open up a channel for thermal fluctuations at $T_c < T < \Delta$, which destabilizes the QAH ground state and reduces the Chern polarization (i.e., destroys the quantized Hall conductivity and recovers the time-reversal symmetry). Only when $T < T_c$, the topological nature of the system manifests, as can be seen in the QMC results of the Berry curvature for a $6 \times 6$ system at $T = 1.25$ meV in Fig. 3(d), if one integrates over the MBZ the obtained $C = 1$.

*Discussion.*—In this study, we show that at $3/4$ filling and $T = 0$, a QAH-TMI state emerges in magic angle TBGs, due to the interplay between flat-band quantum wave functions and Coulomb interactions. In its real-space-model cousin [45], the QAH-TMI ground state only occurs at large $\alpha$, while the presence of the charge density wave (CDW) was seen in a small $\alpha$ region. Our study indicated the QAH-TMI state is the only ground state in the realistic model, while CDW is the result of oversimplification of the real-space model. This QAH-TMI phase melts at a much lower temperature than the zero-temperature gap $\Delta$. We identify that the low-energy excitonic states are the origin of this low transition temperature. At $T_c < T < \Delta$, these excitonic collective modes assist the valence electron to tunnel across the topological band gap, redistribute among the opposite Chern bands, and restore the time-reversal symmetry; such a process generates great enhancement in the charge compressibility, readily detectable via the quantum capacitance measurements. This behavior is qualitatively different from the conventional weakly interacting topological band insulator or correlated lattice models with local interactions. From here, the model computations to fully understand the rich phase diagram away from integer fillings and the nonchiral cases are anticipated in future works.

We thank Xiyue Li, Wei Li, and Tao Shi in the previous collaborations on the real-space TBG model, and Yi Zhang and Jian Kang for discussions on the computation of the Chern number in moiré systems. G. P. P., H. Y. L., X. Z., B. B. C., and Z. Y. M. acknowledge support from the Research Grants Council of Hong Kong SAR of China (Grants No. 17303019, No. 17301420, No. 17301721, No. AoE/P-701/20, and No. 17309822), the Strategic Priority Research Program of the Chinese Academy of Sciences (Grant No. XDB33000000), the K. C. Wong Education Foundation (Grant No. GJTD-2020-01), and the Seed Funding "Quantum-Inspired explainable-AI" at the HKU-TCL Joint Research Centre for Artificial Intelligence. We thank the Computational Initiative at the Faculty of Science and HPC2021 system under the Information Technology Services at the University of Hong Kong, and the Tianhe-II platform at the National Supercomputer Center in Guangzhou for their technical support and generous allocation of CPU time.

*sunkai@umich.edu
†zymeng@hku.hk

[1] G. Trambly de Laissardière, D. Mayou, and L. Magaud, Nano Lett. **10**, 804 (2010).
[2] G. Trambly de Laissardière, D. Mayou, and L. Magaud, Phys. Rev. B **86**, 125413 (2012).
[3] R. Bistritzer and A. H. MacDonald, Proc. Natl. Acad. Sci. U.S.A. **108**, 12233 (2011).
[4] J. M. B. Lopes dos Santos, N. M. R. Peres, and A. H. Castro Neto, Phys. Rev. B **86**, 155449 (2012).
[5] J. M. B. Lopes dos Santos, N. M. R. Peres, and A. H. Castro Neto, Phys. Rev. Lett. **99**, 256802 (2007).
[6] Y. Cao, V. Fatemi, S. Fang, K. Watanabe, T. Taniguchi, E. Kaxiras, and P. Jarillo-Herrero, Nature (London) **556**, 43 (2018).
[7] C. Shen, Y. Chu, Q. Wu, N. Li, S. Wang, Y. Zhao, J. Tang, J. Liu, J. Tian, K. Watanabe, T. Taniguchi, R. Yang, Z. Y. Meng, D. Shi, O. V. Yazyev, and G. Zhang, Nat. Phys. **16**, 520 (2020).
[8] Y. Xie, B. Lian, B. Jäck, X. Liu, C.-L. Chiu, K. Watanabe, T. Taniguchi, B. A. Bernevig, and A. Yazdani, Nature (London) **572**, 101 (2019).

[9] E. Khalaf, S. Chatterjee, N. Bultinck, M. P. Zaletel, and A. Vishwanath, Sci. Adv. **7**, eabf5299 (2021).
[10] K. P. Nuckolls, M. Oh, D. Wong, B. Lian, K. Watanabe, T. Taniguchi, B. A. Bernevig, and A. Yazdani, Nature (London) **588**, 610 (2020).
[11] A. T. Pierce, Y. Xie, J. M. Park, E. Khalaf, S. H. Lee, Y. Cao, D. E. Parker, P. R. Forrester, S. Chen, K. Watanabe *et al.*, Nat. Phys. **17**, 1210 (2021).
[12] Y. Cao, V. Fatemi, A. Demir, S. Fang, S. L. Tomarken, J. Y. Luo, J. D. Sanchez-Yamagishi, K. Watanabe, T. Taniguchi, E. Kaxiras *et al.*, Nature (London) **556**, 80 (2018).
[13] Y. Da Liao, Z. Y. Meng, and X. Y. Xu, Phys. Rev. Lett. **123**, 157601 (2019).
[14] Y.-D. Liao, X.-Y. Xu, Z.-Y. Meng, and J. Kang, Chin. Phys. B **30**, 017305 (2021).
[15] X. Lu, P. Stepanov, W. Yang, M. Xie, M. A. Aamir, I. Das, C. Urgell, K. Watanabe, T. Taniguchi, G. Zhang *et al.*, Nature (London) **574**, 653 (2019).
[16] S. Moriyama, Y. Morita, K. Komatsu, K. Endo, T. Iwasaki, S. Nakaharai, Y. Noguchi, Y. Wakayama, E. Watanabe, D. Tsuya, K. Watanabe, and T. Taniguchi, arXiv:1901.09356.
[17] G. Chen, A. L. Sharpe, E. J. Fox, Y.-H. Zhang, S. Wang, L. Jiang, B. Lyu, H. Li, K. Watanabe, T. Taniguchi *et al.*, Nature (London) **579**, 56 (2020).
[18] A. Rozhkov, A. Sboychakov, A. Rakhmanov, and F. Nori, Phys. Rep. **648**, 1 (2016), electronic properties of graphene-based bilayer systems.
[19] S. Chatterjee, M. Ippoliti, and M. P. Zaletel, Phys. Rev. B **106**, 035421 (2022).
[20] A. Kerelsky, L. J. McGilly, D. M. Kennes, L. Xian, M. Yankowitz, S. Chen, K. Watanabe, T. Taniguchi, J. Hone, C. Dean *et al.*, Nature (London) **572**, 95 (2019).
[21] A. Rozen, J. M. Park, U. Zondiner, Y. Cao, D. Rodan-Legrain, T. Taniguchi, K. Watanabe, Y. Oreg, A. Stern, E. Berg *et al.*, Nature (London) **592**, 214 (2021).
[22] S. L. Tomarken, Y. Cao, A. Demir, K. Watanabe, T. Taniguchi, P. Jarillo-Herrero, and R. C. Ashoori, Phys. Rev. Lett. **123**, 046601 (2019).
[23] T. Soejima, D. E. Parker, N. Bultinck, J. Hauschild, and M. P. Zaletel, Phys. Rev. B **102**, 205111 (2020).
[24] X. Liu, C.-L. Chiu, J. Y. Lee, G. Farahi, K. Watanabe, T. Taniguchi, A. Vishwanath, and A. Yazdani, Nat. Commun. **12**, 1 (2021).
[25] E. Khalaf, N. Bultinck, A. Vishwanath, and M. P. Zaletel, arXiv:2009.14827.
[26] U. Zondiner, A. Rozen, D. Rodan-Legrain, Y. Cao, R. Queiroz, T. Taniguchi, K. Watanabe, Y. Oreg, F. von Oppen, A. Stern, E. Berg, P. Jarillo-Herrero, and S. Ilani, Nature (London) **582**, 203 (2020).
[27] Y. Saito, F. Yang, J. Ge, X. Liu, T. Taniguchi, K. Watanabe, J. I. A. Li, E. Berg, and A. F. Young, Nature (London) **592**, 220 (2021).
[28] A. Ghiotto, E.-M. Shih, G. S. S. G. Pereira, D. A. Rhodes, B. Kim, J. Zang, A. J. Millis, K. Watanabe, T. Taniguchi, J. C. Hone, L. Wang, C. R. Dean, and A. N. Pasupathy, Nature (London) **597**, 345 (2021).
[29] F. Schindler, O. Vafek, and B. A. Bernevig, Phys. Rev. B **105**, 155135 (2022).
[30] L. Wang, E.-M. Shih, A. Ghiotto, L. Xian, D. A. Rhodes, C. Tan, M. Claassen, D. M. Kennes, Y. Bai, B. Kim, K. Watanabe, T. Taniguchi, X. Zhu, J. Hone, A. Rubio, A. N. Pasupathy, and C. R. Dean, Nat. Mater. **19**, 861 (2020).
[31] J. M. Park, Y. Cao, K. Watanabe, T. Taniguchi, and P. Jarillo-Herrero, Nature (London) **592**, 43 (2021).
[32] Y. D. Liao, J. Kang, C. N. Breiø, X. Y. Xu, H.-Q. Wu, B. M. Andersen, R. M. Fernandes, and Z. Y. Meng, Phys. Rev. X **11**, 011014 (2021).
[33] L. An, X. Cai, D. Pei, M. Huang, Z. Wu, Z. Zhou, J. Lin, Z. Ying, Z. Ye, X. Feng, R. Gao, C. Cacho, M. Watson, Y. Chen, and N. Wang, Nanoscale Horiz. **5**, 1309 (2020).
[34] M. Huang, Z. Wu, J. Hu, X. Cai, E. Li, L. An, X. Feng, Z. Ye, N. Lin, K. T. Law, and N. Wang, Natl. Sci. Rev. nwac232 (2022), 10.1093/nsr/nwac232.
[35] E. Li, J.-X. Hu, X. Feng, Z. Zhou, L. An, K. T. Law, N. Wang, and N. Lin, Nat. Commun. **12**, 5601 (2021).
[36] L. Rademaker, D. A. Abanin, and P. Mellado, Phys. Rev. B **100**, 205114 (2019).
[37] F. Guinea and N. R. Walet, Proc. Natl. Acad. Sci. U.S.A. **115**, 13174 (2018).
[38] N. N. T. Nam and M. Koshino, Phys. Rev. B **96**, 075311 (2017).
[39] S. Carr, S. Fang, Z. Zhu, and E. Kaxiras, Phys. Rev. Res. **1**, 013001 (2019).
[40] X. Zhang, K. Sun, H. Li, G. Pan, and Z. Y. Meng, Phys. Rev. B **106**, 184517 (2022).
[41] G. Wagner, Y. H. Kwan, N. Bultinck, S. H. Simon, and S. A. Parameswaran, Phys. Rev. Lett. **128**, 156401 (2022).
[42] S. Zhang, X. Lu, and J. Liu, Phys. Rev. Lett. **128**, 247402 (2022).
[43] J. Liu and X. Dai, Phys. Rev. B **103**, 035427 (2021).
[44] B.-B. Chen, Y. D. Liao, Z. Chen, O. Vafek, J. Kang, W. Li, and Z. Y. Meng, Nat. Commun. **12**, 5480 (2021).
[45] X. Lin, B.-B. Chen, W. Li, Z. Y. Meng, and T. Shi, Phys. Rev. Lett. **128**, 157201 (2022).
[46] G. Pan, W. Jiang, and Z. Y. Meng, arXiv:2207.02123.
[47] J. Kang and O. Vafek, Phys. Rev. Lett. **122**, 246401 (2019).
[48] M. Koshino, N. F. Q. Yuan, T. Koretsune, M. Ochi, K. Kuroki, and L. Fu, Phys. Rev. X **8**, 031087 (2018).
[49] H. C. Po, L. Zou, A. Vishwanath, and T. Senthil, Phys. Rev. X **8**, 031089 (2018).
[50] S. Raghu, X.-L. Qi, C. Honerkamp, and S.-C. Zhang, Phys. Rev. Lett. **100**, 156401 (2008).
[51] Y. Jia, H. Guo, Z. Chen, S.-Q. Shen, and S. Feng, Phys. Rev. B **88**, 075101 (2013).
[52] S. Capponi and A. M. Läuchli, Phys. Rev. B **92**, 085146 (2015).
[53] X. Zhang, G. Pan, Y. Zhang, J. Kang, and Z. Y. Meng, Chin. Phys. Lett. **38**, 077305 (2021).
[54] G. Pan, X. Zhang, H. Li, K. Sun, and Z. Y. Meng, Phys. Rev. B **105**, L121110 (2022).
[55] J. S. Hofmann, E. Khalaf, A. Vishwanath, E. Berg, and J. Y. Lee, Phys. Rev. X **12**, 011061 (2022).
[56] X. Zhang, G. Pan, B.-B. Chen, H. Li, K. Sun, and Z. Y. Meng, arXiv:2210.11733.
[57] H. Li, U. Kumar, K. Sun, and S.-Z. Lin, Phys. Rev. Res. **3**, L032070 (2021).
[58] P. Rickhaus, M.-H. Liu, M. Kurpas, A. Kurzmann, Y. Lee, H. Overweg, M. Eich, R. Pisoni, T. Taniguchi, K. Watanabe,

K. Richter, K. Ensslin, and T. Ihn, Sci. Adv. **6**, eaay8409 (2020).
[59] Z.-D. Song, B. Lian, N. Regnault, and B. A. Bernevig, Phys. Rev. B **103**, 205412 (2021).
[60] B. A. Bernevig, Z.-D. Song, N. Regnault, and B. Lian, Phys. Rev. B **103**, 205413 (2021).
[61] Y. Zhang, K. Jiang, Z. Wang, and F. Zhang, Phys. Rev. B **102**, 035136 (2020).
[62] B. A. Bernevig, B. Lian, A. Cowsik, F. Xie, N. Regnault, and Z.-D. Song, Phys. Rev. B **103**, 205415 (2021).
[63] S. Liu, E. Khalaf, J. Y. Lee, and A. Vishwanath, Phys. Rev. Res. **3**, 013033 (2021).
[64] J. M. Pizarro, M. Rösner, R. Thomale, R. Valentí, and T. O. Wehling, Phys. Rev. B **100**, 161102(R) (2019).
[65] X. Zhang, G. Pan, X. Y. Xu, and Z. Y. Meng, Phys. Rev. B **106**, 035121 (2022).
[66] G. Pan and Z. Y. Meng, arXiv:2204.08777.
[67] Z. Yan and Z. Y. Meng, arXiv:2112.05886.
[68] C. Zhou, Z. Yan, H.-Q. Wu, K. Sun, O. A. Starykh, and Z. Y. Meng, Phys. Rev. Lett. **126**, 227201 (2021).
[69] Z. Yan, Y.-C. Wang, N. Ma, Y. Qi, and Z. Y. Meng, npj Quantum Mater. **6**, 39 (2021).
[70] Z. Wang and S.-C. Zhang, Phys. Rev. X **2**, 031008 (2012).
[71] T. Fukui, Y. Hatsugai, and H. Suzuki, J. Phys. Soc. Jpn. **74**, 1674 (2005).
[72] See Supplemental Material at http://link.aps.org/supplemental/10.1103/PhysRevLett.130.016401 for detailed QMC implementation of the TBG model and the analyses of their polynomial sign problem and the implementation of different physical observables.
[73] P. J. Ledwith, G. Tarnopolsky, E. Khalaf, and A. Vishwanath, Phys. Rev. Res. **2**, 023237 (2020).
[74] M.-R. Li, A.-L. He, and H. YaoarXiv:2111.12107.
[75] R. Mondaini, S. Tarat, and R. T. Scalettar, Science **375**, 418 (2022).